THE JOURNAL OF PHYSICAL CHEMISTRY C

Article

Cite This: J. Phys. Chem. C 2019, 123, 29173−29183

pubs.acs.org/JPCC

Deformation and Swelling of Kerogen Matrix in Light Hydrocarbons and Carbon Dioxide

Stéphane Tesson[†,‡] and Abbas Firoozabadi*[,†,§]

[†]Reservoir Engineering Research Institute, 595 Lytton Avenue, Suite B, Palo Alto, California 94301, United States

[‡]Department of Chemical and Environmental Engineering, University of California—Riverside, Riverside, California 92521, United States

[§]Department of Chemical and Biomolecular Engineering, Rice University, Houston, Texas, 77005, United States

Supporting Information

ABSTRACT: Shale gas has become an attractive alternative to conventional fossil fuels due to its clean-burning characteristics. Fluid molecules reside in micropores and mesopores in shale formations. Molecular simulations provide insights into the kerogen structures, adsorption of hydrocarbons and carbon dioxide, and kerogen swelling. In this work, a new approach is introduced to create atomistic configurations of kerogen matrix with specific porosity. A dummy particle is used to control the porosity. Once the kerogen matrix is created, the dummy particle is removed and a limited number of nails are placed on the periphery of the pores to prevent the kerogen matrix from collapsing and to keep its basic structure intact. The hybrid Molecular Dynamics-Grand Canonical Monte Carlo (MD-GCMC) simulations are performed to investigate the adsorption and kerogen swelling of five hydrocarbon gases (methane, ethane, propane, *n*-butane, and *i*-butane at 393.15 K and various pressures), *n*-pentane liquid (at 298.15 K and 1 atm), and supercritical carbon dioxide (at 393.15 K to a pressure of 400 atm). The kerogen matrix is flexible. Our simulation results show that there is a coupling between adsorbate molecular size and shape and deformation of the kerogen matrix structure. The flexibility of the kerogen matrix affects swelling. The kerogen matrix deformation allows small adsorbate molecules to dissolve in the matrix. Our simulations results show that kerogen swelling decreases with the increase of the molecular size of the adsorbate (CO_2 > CH_4 > C_2H_6 > C_3H_8). The deformation and increase in swelling by *n*-pentane is much more pronounced than by methane and other light hydrocarbon gases. Our work is based on type II-A kerogen macromolecules. The methodology can be applied to other types of kerogen molecules.

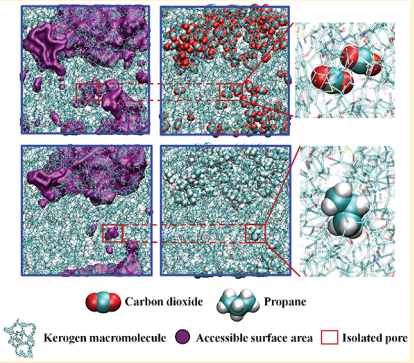

INTRODUCTION

Shale gas has changed the energy landscape of the conventional fossil fuels. Natural gas is a clean-burning fuel and produces less CO_2 compared to crude oil. The United States (U.S.) has become the major shale gas producer in the world. In 2017, the total production of dry natural gas was about 17 trillion cubic feet (Tcf) per year from shale resources in the U.S. This corresponds to 62% of total U.S. dry natural gas production in that year.[1] Despite the high production of hydrocarbons from shale oil/gas reservoirs, the recovery factor is very low. A better understanding of the shale physicochemical properties may lead to new processes to improve shale gas recovery as well as advancing the environmental stewardship.

Shale rock is composed of inorganic minerals and organic matter. The organic matter is mainly composed of kerogens. Kerogen is insoluble in common polar solvents;[2] it is essentially composed of polydisperse macromolecules. Shale gas resides in micropores and mesopores.[3,4] The fluids in the kerogen matrix can be in three different states: (i) adsorbed state on the kerogen surface, (ii) free molecules in the pores, and (iii) dissolved molecules in the kerogen matrix.[5] The physicochemical properties of kerogen depend on its origin and on its burial history.[6,7] Different kerogen types[8−10] can be distinguished: (i) type I from a lacustrine anoxic environment, (ii) type II from marine shale and continental planktons, (iii) type III from plants in tertiary and quaternary coals, and (iv) type IV from older sediments redeposited after erosion. In the geological medium, kerogen is exposed to constraints such as temperature and pressure. Under these conditions the type of kerogen affects the microstructure and on the fluid behavior confined in kerogen pores. The interplay between gas adsorption, structural deformation, and the swelling and shrinkage of the kerogen may relate to increase in shale gas production. This interplay is not well understood. The adsorption and swelling of kerogen media by gases (CH_4, C_2H_6, C_3H_8, n−C_4H_{10}, i−C_4H_{10} and CO_2) and liquid n−C_5H_{12} is the focus of this work.

Adsorption is strongly linked to the accessible surface area and the porosity. Experimental research has mostly focused on adsorption in shale samples.[11−22] Recent studies investigate the

Received: May 14, 2019
Revised: October 28, 2019
Published: November 5, 2019

DOI: 10.1021/acs.jpcc.9b04592
J. Phys. Chem. C 2019, 123, 29173−29183

adsorption of light hydrocarbon gases (CH_4, C_2H_6, C_3H_8, n−C_4H_{10} and i−C_4H_{10}) and carbon dioxide in isolated kerogen.[17,23−27] Kerogen pore structure may deform from gas adsorption. The fluids may dissolve in the kerogen, adding to swelling. Extensive experimental studies on kerogen swelling in several liquid hydrocarbons have been reported at room temperature and atmospheric pressure.[28−36] The measurements reveal that (i) the swelling decreases as the maturity of the rock increases, (ii) the effect of temperature is not as pronounced as maturity, and (iii) samples prepared by pretreatment temperature swell differently compared to nontreated samples. Larsen and Li[28,30] (kerogen type I and II), Larsen et al.[31] (different kerogen types II) and Ballice et al.[32] (kerogen type I and II) use the volumetric swelling method to measure the swelling of kerogen by n−C_5H_{12} at room temperature and atmospheric pressure. They find the kerogen samples swell from 15 to 24%. The measurements at high pressure are a challenge.

Molecular simulations have also been used to predict swelling. Many computational investigations have been performed to provide insights into kerogen structural properties,[7,37−54] kerogen adsorption properties,[7,39,46−50,52,53,55−62] but swelling of kerogen has been studied in a limited number of studies.[7,43,44,49,53]

Three different methods have been used to create kerogen matrix. In one method, the kerogen macromolecules are placed in a box without other species.[7,46−48,50] In another method, the kerogen macromolecules are placed in a box with specific molecules.[39,42,45,54,55,63,64] In a third method, a hybrid reverse Monte Carlo reconstruction technique is used.[37,38,40,51] MD simulations are used for the creation of the initial kerogen structure in the studies mentioned below. Sui and Yao[7] create the kerogen matrix using 6 kerogen macromolecules of type II-A at T = 300 K and P = 10 atm. They calculate methane accessible surface area of 1548 m^2g^{-1} and pore volume of 0.181 cm^3g^{-1}. They also estimate carbon dioxide accessible surface area of 1845 m^2g^{-1} and pore volume of 0.209 cm^3g^{-1}. Pathak et al.[43] and Pathak et al.[44] create the kerogen matrix, respectively, using 35 and 15 kerogen macromolecules of type II−C at T = 300 K and P = 300 atm. Pathak et al.[43] do not report the porosity and the accessible surface area. Pathak et al.[44] use a Monte Carlo integration method to report porosity[65] of 3.7%. Wang et al.[53] create the kerogen matrix using 10 kerogen macromolecules of type I-A at T = 300 K and P = 197 atm. Ho et al.[49] create the kerogen matrix using 27 kerogen macromolecules of type II-D at T = 300 K and P = 1 atm. They calculate a porosity close to 26% (based on helium probe particles) and an increase of the accessible surface area (from ∼3% at 1 atm to ∼8% at 192 atm for methane and from ∼6% at 1 atm to ∼18% at 192 atm for CO_2). However, other authors[39,44,45,55,62,66] report a lower porosity, pore volume, and accessible surface area. Collell et al.,[55] Michalec and Lisal,[39] Kazemi et al.[66] and Vasileiadis et al.[45] report a porosity ranging from 0.7 to 2% and an accessible surface area ranging from 4.7 to 232 m^2g^{-1}. Trewin et al.[67] point out that a scaling factor should be applied to the calculated accessible surface area and pore volume from the Connolly method to obtain true values. They show that the Connolly method overestimates the accessible surface area and the pore volume. One of the objectives of this investigation is the creation of flexible kerogen matrix to investigate the adsorption of hydrocarbon gases from methane to *n*-butane and CO_2. In particular, we are interested to examine the 50% difference in adsorption of *n*-butane and *i*-butane measured by Zhao et al.[24,25] and Wu et al.[26]

Swelling of kerogen matrix has been investigated by three different methods: (i) the poromechanical model[68,69] (using fixed kerogen volume), (ii) the molecular dynamics simulations, and (iii) the hybrid molecular dynamics-grand canonical Monte Carlo (MD-GCMC) method. Sui and Yao[7] and Wang et al.[53] apply the poromechanical method. They use GCMC simulations to calculate methane and carbon dioxide adsorption isotherms at T = 298, 340, and 380 K and P to 296 atm (Sui and Yao[7]) and T = 298, 328, 358, and 388 K and P = 296 atm (Wang et al.[53]). Sui and Yao[7] observe that the volumetric strain increases until reaching a plateau. They find that the maximum swellings of kerogen by methane and carbon dioxide are, respectively, 4.45% and 6.52% at 340 K and 148 atm. Wang et al.[53] observe a different trend. The volumetric strain first increases up to a maximum as pressure increases, and then decreases gradually with further pressure increase. They find that the maximum swelling of kerogen by methane is 1.20% (at 298 K and 158 atm), 0.75% (at 328 K and 128 atm), 0.55% (at 358 K and 128 atm), and 0.3% (at 388 K and 89 atm). Pathak et al.[44] use MD simulations to study the swelling of a type II−C kerogen matrix at 400 K and 300 atm. They investigate four different cases: (i) pure kerogen in order to calculate the volume of the simulation box without adsorbate ($V_{\text{kerogen w/o adsorbate}}$), (ii) 15 kerogen molecules with 750 methane molecules, (iii) 15 kerogen molecules with 750 carbon dioxide molecules, and (iv) 15 kerogen molecules with CH_4 and CO_2 molecules (in a 1:3 molecular ratio with a total of 750 molecules). They find that the swelling of kerogen by methane, carbon dioxide and CH_4 and CO_2 mixture is, respectively, 74%, 54%, and 54%. Note that in this method swelling may be a function of mixing of the number of molecules. Pathak et al.[43] use the same methodology to investigate the swelling of a type II−C kerogen matrix by different liquids (based on a fixed mass of kerogen and a 20% mass of liquid hydrocarbons) at 300 and 375 K and 1 and 300 atm. They observe that different liquid hydrocarbons swell kerogen differently; the swelling is more pronounced by polar and aromatic hydrocarbons than by other liquids. Ho et al.[49] use the MD-GCMC method to investigate the swelling of a type II-D kerogen matrix by methane, carbon dioxide, and helium at T = 300 K and P to 192 atm. They report that the volumetric strain increases with increasing pressure and it is less than 0.5%, 5.4% and 11% when calculated by He, CH_4, and CO_2, respectively, at T = 300 K and P = 192 atm. There are various evidence that adsorption and swelling are affected by flexibility of kerogen matrix.[62,70] One objective of this investigation is further study of adsorption and swelling of kerogen matrix to a pressure of 400 atm. Another objective is the investigation of adsorption of *n*-C_4H_{10} and *i*-C_4H_{10} because of the significant difference in adsorption measurements of the two fluids.

We aim to investigate swelling in gases (methane, ethane, propane, *n*-butane, *i*-butane, and carbon dioxide) and liquid *n*-pentane based on molecular simulations of fully flexible macromolecules. A key point of this investigation is to find out the difference in swelling, and pore struture deformation in gases and liquids. The manuscript is organized as follows. After the introduction, the kerogen, hydrocarbons, and CO_2 molecular models are provided as well as the computational details. Then, the process to create the kerogen matrix is presented. Next, we investigate adsorption of each adsorbate

DOI: 10.1021/acs.jpcc.9b04592
J. Phys. Chem. C 2019, 123, 29173−29183

and the swelling and the kerogen matrix deformation. At the end, we draw conclusions.

MATERIALS AND METHODS

Atomistic Models. Type II-A kerogen macromolecule ($M_{C_{252}H_{294}O_{24}N_6S_3}$ = 3887 g mol^{-1} proposed by Ungerer et al.[2]), dummy particle (σ_{DP} = 33 Å), probe particles nitrogen (σ_{N_2} = 3.653 Å), and helium (σ_{He} = 2.9 Å), various hydrocarbon gases (methane, ethane, propane, *n*-butane, and *i*-butane), liquid *n*-pentane and carbon dioxide are included in this study. The graphical user interface (GUI) of the MedeA software environment[71] (version 2.21) is used to create a fully flexible kerogen matrix. The kerogen matrix has a chemical composition close to the isolated kerogen samples used in adsorption measurements in our laboratory.[24−26] All the species are illustrated in Figure 1 and the physicochemical

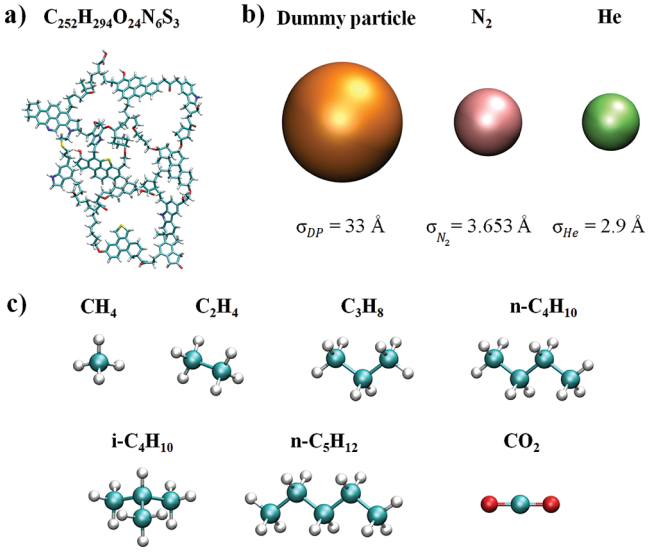

Figure 1. (a) Type II-A kerogen macromolecule. (b) Dummy particle and probe particles He and N_2. (c) Molecular structure of methane, ethane, propane, *n*-butane, *i*-butane, *n*-pentane, and the carbon dioxide. Color code: cyan (C), white (H), red (O), yellow (S), blue (N), orange (DP), pink (N_2) and lime (He). The dummy particle and probe particles are represented by a single sphere.

properties of the type II-A kerogen are listed in Table S1 in the Supporting Information (SI). In this work, one dummy particle is introduced to create large pores and a porosity of around 10%. Probe particles He and N_2 are used to calculate the accessible surface area and porosity, respectively.

Simulation Methods. The polymer consistent force field plus (PCFF+)[71−74] is used to model all the molecules. PCFF+ is an all atom force field developed by Materials Design[71] to study the properties of organic matter including polymers and kerogens with high accuracy. It is a second generation force field belonging to the family of the consistent force field (such as the condensed-phase optimized molecular potentials for atomistic simulation studies force field[75−79] (COMPASS)). The total potential consists of seven terms:

$$V_{total} = V_{bonds} + V_{angles} + V_{dihedrals} + V_{impropers} + V_{crossterms} + V_{charges} + V_{vdW} \quad (1)$$

The first five terms (V_{bonds}, V_{angles}, $V_{dihedrals}$, $V_{impropers}$, and $V_{crossterms}$) represent the bonding interactions, and the last two terms ($V_{charges}$ and V_{vdW}) account for the nonbonding interactions between atomic pairs. The van der Waals interactions are calculated with a cutoff distance of 9.5 Å, and the van der Waals cross terms are derived from the Wäldman and Hagler combining rules.[80] The electrostatic interactions are computed using the Ewald summation.[81]

Molecular dynamics (MD) simulations are performed in the canonical (NVT) and isothermal−isobaric (NPT) ensemble in order to create kerogen matrix. The NPT ensemble is used to investigate adsorption and swelling of the kerogen matrix. MD simulations are applied by using the large-scale atomic molecular massively parallel simulator (LAMMPS) software[82] (stable version 31st March 2017). The time steps are, respectively, 1.0 and 0.1 fs in MD simulations in the NVT and NPT ensembles. The periodic boundary conditions (PBC) are applied in the three directions of space. The temperature and the pressure are, respectively, controlled by the Nosé−Hoover thermostat[83,84] and barostat[85,86] with a relaxation time of 1 ps.

The hybrid MD-GCMC method[87] implemented in LAMMPS is used to investigate adsorption of CO_2 and hydrocarbons and the swelling of the kerogen matrix. The MD-GCMC method is performed as follows: a GCMC cycle including 2500 GCMC exchanges (addition and deletion are each attempted with 50% probability) and 2500 GCMC moves (translation and rotation are each attempted with 50% probability) are performed after every 10 000 MD steps. In GCMC simulations, pressure and fugacity coefficient are required as input. As in our previous work,[62] we calculated the fugacity coefficient using the Thermosolver software[88,89] (GCMC simulations are performed to verify that the experimental density of each substance studied agrees with the one predicted by the force field. The results are presented in Table S2). After each GCMC simulation, the number of atoms changes in the simulation box, therefore the number of atoms is updated before each MD simulations. The MD simulations are carried in the NPT ensemble using the same time step, thermostat and barostat as stated above. They allow kerogen and gas molecules to relax. Therefore, the system is free to shrink or swell during the MD simulations. The hybrid simulation characteristics are listed in Table S3 in the SI.

Characterization Methods. We use the same methods in this work as in Tesson and Firoozabadi[62] to calculate the porosity, accessible surface area (S_{acc}), and pore size distribution (PSD). In the following, a summary is presented.

- The porosity is computed by the Herrera et al.[65] method. The principle consists of inserting probe molecules randomly inside the simulation box. If the inset probe molecule does not overlap with the kerogen atoms, then the insertion is accepted, otherwise it is rejected.
- The accessible surface area is calculated by the Düren et al.[90] method. The principle consists of rolling the probe molecule on the surface of the pores of the kerogen matrix.
- The pore size distribution is obtained by the Bhattacharya and Gubbins[91] method. The principle is based on inserting particles randomly in the simulation box, increasing their size, and determining the largest sphere from the center of mass of probe molecule to the surface of the pores.
- The volumetric strain is defined as follows:

DOI: 10.1021/acs.jpcc.9b04592
J. Phys. Chem. C 2019, 123, 29173−29183

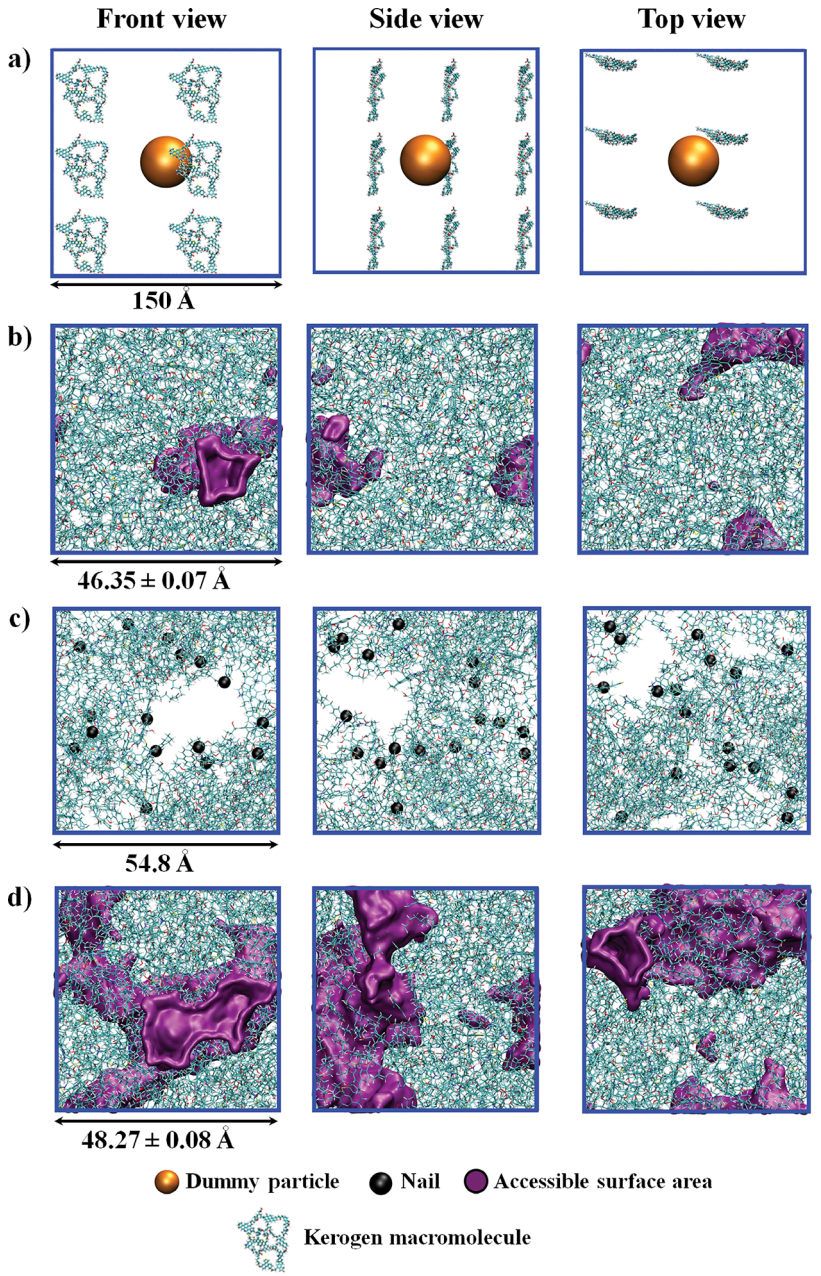

Figure 2. Front, side, and top view of the simulation box at different stages of the molecular dynamics relaxation procedure. (a) Initial orthorhombic simulation box of dimensions 150 × 150 × 150 Å^3. (b) Accessible surface area of the final simulation box without nails at T = 298.15 K and P = 1 atm. (c) Initial simulation box of stage 9 of the MD relaxation procedure in which the 17 nailed atoms are highlighted in black. (d) Accessible surface area of the final simulation box with nails: T = 298.15 K and P = 1 atm.

$$Q_v = \frac{V_{\text{box with kerogen and adsorbate}} - V_{\text{box with kerogen and w/o adsorbate}}}{V_{\text{box with kerogen and w/o adsorbate}}} \quad (2)$$

where $V_{\text{box with kerogen and adsorbate}}$ and $V_{\text{box with kerogen and w/}o\ adsorbate}$ are, respectively, the volume of the swollen and initial simulation box.

The porosity and accessible surface area are calculated by helium (σ_{He} = 2.9 Å) and nitrogen (simplified by a single sphere with σ_{N_2} = 3.653 Å) probe molecules, respectively. The nitrogen molecule is simplified by a single sphere.

KEROGEN MATRIX

Creation. Kerogen matrix is created using the graphical user interface (GUI) of the MedeA software.[71] The force field parameters are applied and the kerogen molecules are relaxed by "simple force field minimization" and "simple force field dynamics" of MedeA modules. Seventeen kerogen macromolecules and one dummy particle (σ_{DP} = 33 Å) are placed inside an orthorhombic cell of dimensions 150 × 150 × 150 Å^3 (initial cell density is 0.03 g cm^{-3}). The initial configuration is shown in Figure 2a. Our MD relaxation procedure is applied; the process is summarized in Table 1. In contrast to our previous work,[62] we add a refinement stage (stage 9) in which the dummy particle is removed and a simulation of 100 ns in the NPT ensemble is performed in order to relax the system. We find that the pore system collapses. At the beginning of stage 9, the porosity is ∼30%, after 100 ns, it reduces to 1.7 ± 0.1%. The accessible surface area after the pore collapse is

DOI: 10.1021/acs.jpcc.9b04592
J. Phys. Chem. C 2019, 123, 29173−29183

Table 1. Molecular Dynamics Relaxation Procedure to Create the Flexible Kerogen Matrix[a]

stage	ensemble	temperature (K)	pressure (atm)	time (ns)
1	NVT	298.15		1
2	NVT	298.15 → 1000		1
3	NVT	1000		1
4	NPT	1000 → 700	100	1
5	NPT	700 → 500	100	1
6	NPT	500 → 298.15	100	1
7	NPT	298.15	100 → 1	1
8	NPT	298.15	1	10
9	NPT	298.15	1	100

[a]Before starting stage 9, the dummy particle is removed and the nails are placed in the periphery of the large pores.

shown in Figure 2b (also listed in Table 2). The structure characteristics are provided in Table 2 and the PSD is presented in Figure S1. The pores are small and cannot host propane, *n*-butane, *i*-butane, and *n*-pentane. To prevent the pore collapse and to create a kerogen matrix with a high porosity (over 10%) we examine three different processes. In two of the methods in addition to kerogen molecules we place, at the beginning of stage 1, inside the simulation box: (i) 12 asphaltene/resin molecules from Collell et al.,[64] in the other (ii) 21 immature asphaltene molecules from León-Barreneche et al.[92] The asphaltene/resin and asphaltene molecules are used to fill the small pores to keep the large pores intact at the end of the MD relaxation process. The pore system collapses in these two methods.

In the third approach, at the beginning of stage 9, we nail a limited number of atoms. The nails are located at the periphery of the pores. The position and the number of the nails are selected to provide a porosity of about 10%. A small number of nails is used to keep the structure flexible. Carbon atoms located at the center of different polyaromatic clusters in kerogen macromolecules are used as nail centers. The nailed atoms (located at the rigid part of the molecule) will act as a ball joint and the polyaromatic cluster as a barrier preventing the shrinkage of the pore. In this work, at the beginning of stage 9, we examine different number of nails. Among different number of nails we select 17 nails. All the 17 kerogen macromolecules have at least one part in contact with the largest pore. However, only 15 kerogen macromolecules have polyaromatic clusters located at the periphery of the largest pore (13 kerogen macromolecules have one nailed atom and 2 have two nailed atoms). During the simulation, the nailed atoms are not included in the time integration to hold these atoms stationary. The nailed atoms are depicted in Figures 2c and S2. The nailing allows the high porosity from the pressure increase to be kept; the system does not collapse. The accessible surface area (after implementation of nailing) is shown in Figure 2d and the structure characteristics are provided in Table 2 (they are also reported as a function of the number of nails in Table S4).

Reversibility of Structural Properties and *n*-Pentane Swelling. First, we analyze the microstructure of the nailed kerogen matrix at 298.15 K to a pressure of 200 atm without adsorbate to investigate the effect of pressure on structure integrity. MD simulations are performed in the NPT ensemble for 10 ns. We find that the porosity, accessible surface area, and pore size distribution (Figure S1 and Table S5) are not significantly afftected by the pressure increase. The box size and skeletal density increase with pressure increase, whereas the porosity and accessible surface area decrease with pressure increase. The structural changes of the kerogen matrix are reversible in the nailed kerogen matrix.

Then, we examine *n*-pentane swelling in the nailed kerogen matrix at 298.15 K and 1 atm to verify the model. The structural properties are presented in Table 3, and the pore size distribution and *n*-pentane accessible surface area are, respectively, presented in panels 3a, 3b, and 3c of Figure 3. The results show that the lattice, porosity, and accessible surface area increase, respectively, from 48.27 ± 0.08 Å, 10.8 ± 0.2%, and 360 ± 11 $m^2\ g^{-1}$ to 49.9 ± 0.3 Å, 16.0 ± 0.6%, and 698 ± 21 $m^2\ g^{-1}$. The resulting volumetric strain is about 9%. The calculated volumetric strain is lower than the experimental data[28,30−32] which is between 15 and 24%. The 9% increase from our simulations show that the nailed kerogen can describe the swelling. There is a shift in the pore size distribution to larger pores from the introduction of *n*-pentane to kerogen matrix (Figure 3a). By analyzing the trajectory, we find that the matrix deforms and paths are created allowing the *n*-pentane molecules to go back and forth from one pore to another (Figures 3b and c).

RESULTS AND DISCUSSION

Adsorption and Kerogen Swelling. We analyze gas adsorption isotherms in flexible kerogen matrix at T = 393.15 K to a pressure of 400 atm by carbon dioxide, methane, ethane, and propane, and to a pressure of 20 atm for *n*-butane and *i*-butane. The adsorption isotherms are calculated following a sequential method, i.e., the starting configuration of each pressure is the final configuration of the previous one. For each thermodynamic point and for all systems we have verified that the equilibrium is reached by examining temperature, pressure and loading (results for *n*-butane at 20 atm are presented in Figure S4). The density of each system is presented in Table S6. (Note that the density increase from CO_2 adsorption and dissolution in kerogen matrix is more than hydrocarbons including *n*-C_5H_{12}. The increase from CO_2 dissolution is in line with density increase of hydrocarbon liquids from dissolution of CO_2.[93]) The adsorption affects swelling in a flexible kerogen matrix. We also have verified the effect of the nails on the structural properties by a direct method. The CH_4 and CO_2 adsorption isotherms at T = 393.15 K and P = 400 atm are calculated based on the starting configuration from the

Table 2. Structure Characterization of the Kerogen Matrix at the End of the MD Relaxation Procedure (T = 298.15 K and P = 1 atm) without and with 17 Nails[a]

system	lattice (Å)	box density (g cm^{-3})	skeletal density (g cm^{-3})	porosity (%)	accessible surface area ($m^2\ g^{-1}$)
w/o nail	46.35 ± 0.07	1.102 ± 0.005	1.121 ± 0.004	1.7 ± 0.1	103 ± 8
with nails	48.27 ± 0.08	0.976 ± 0.005	1.055 ± 0.004	10.8 ± 0.2	360 ± 11

[a]The skeletal density is based on the volume measured excluding the pores and the void spaces between particles.

DOI: 10.1021/acs.jpcc.9b04592
J. Phys. Chem. C 2019, 123, 29173−29183

Table 3. Structure Characterization of the Nailed Kerogen Matrix from Saturation by Liquid *n*-Pentane at T = 298.15 K and P = 1 atm

lattice (Å)	porosity (%)	accessible surface area ($m^2\ g^{-1}$)	total uptake ($\times 10^{-3}$ mmol m^{-2})	Q_s (%)
49.9 ± 0.3	16.0 ± 0.6	698 ± 21	2.49	9

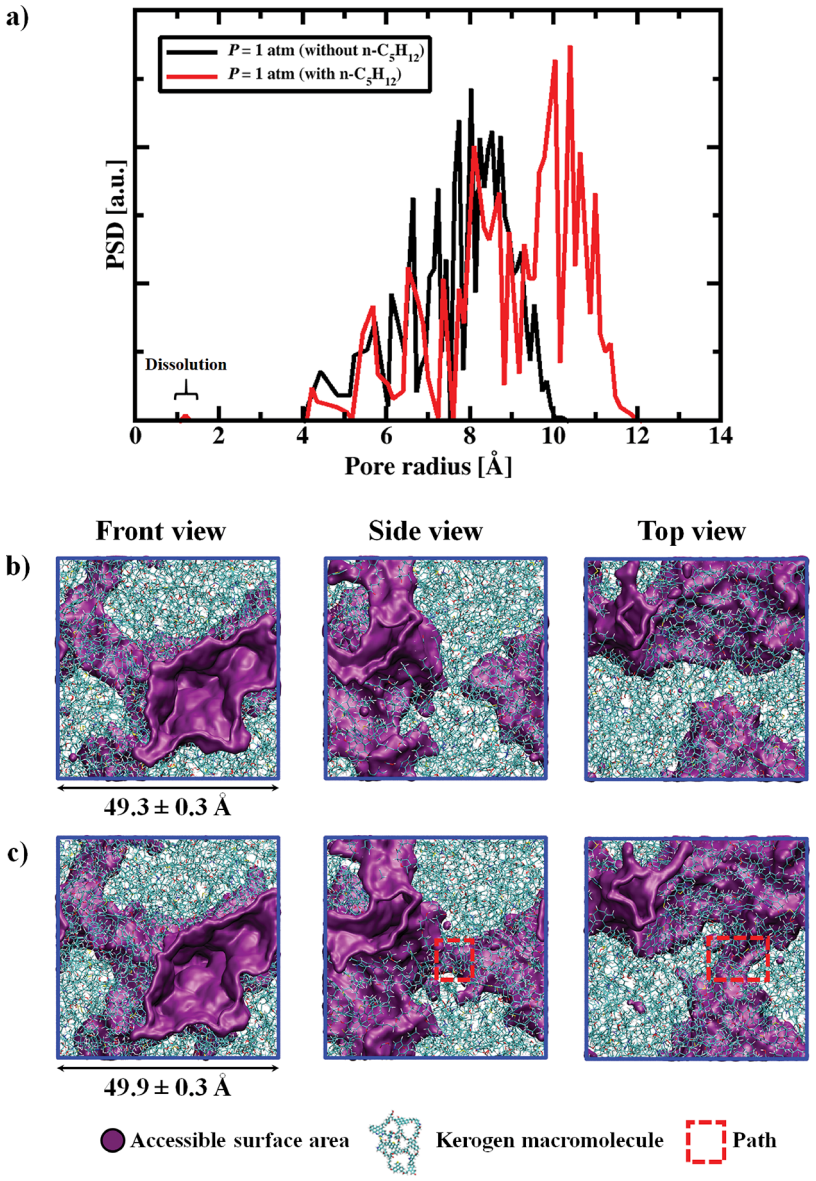

Figure 3. Pore size distribution and views from front, side, and top of the nailed simulation box after *n*-pentane saturation. (a) Pore size distribution before (black line) and after (red line) *n*-pentane saturation. Accessible surface area (b) before saturation by *n*-pentane, and (c) after saturation by *n*-pentane (in the nailed kerogen): T = 298.15 K and P = 1 atm.

final configuration of the MD relaxation procedure. The properties calculated by the direct and sequential methods are close. They are presented in Table S7.

Figure 4a shows that the total uptake reaches a plateau, of 3.58×10^{-3} mmol m^{-2} by ethane at ∼200 atm; 3.66×10^{-3} mmol m^{-2} by propane at ∼100 atm; 2.13×10^{-3} mmol m^{-2} by *n*-butane at ∼15 atm and 1.52×10^{-3} mmol m^{-2} by *i*-butane at ∼15 atm. The temperature is 393.15 K. The total uptake of carbon dioxide (6.37×10^{-3} mmol m^{-2} at 400 atm) and methane (4.15×10^{-3} mmol m^{-2} at 400 atm) have increasing trend between 1 and 400 atm. The trends are consistent with absolute adsorption results based on measurement of excess adsorptions.[25,26,94] The trends are also consistent with molecular simulation results by Collell et al.[55] (methane and ethane), Sui et al.[7] (methane and carbon dioxide), Vasileiadis et al.[52] (methane, ethane, *n*-butane, and carbon dioxide) in rigid kerogen matrices. Ho et al.[49] (methane, carbon dioxide, and helium), Tesson and Firoozabadi[62] (methane), and Wu and Firoozabadi[70] (methane) show also the same trends in flexible kerogen matrices. The total uptake of CO_2 is ∼1.7 times higher (in mol) than the total uptake of CH_4 at 393.15 K and 200 atm. The result has the same trend as found by Ho et al.[49] in type II-D kerogen matrix (the total uptake of CO_2 is ∼1.6 times higher than the total uptake of CH_4 at 300 K and 192 atm). Figure 4a indicates that the *n*-butane adsorption is about ∼1.5 times higher than the *i*-butane adsorption at 393.15

DOI: 10.1021/acs.jpcc.9b04592
J. Phys. Chem. C 2019, 123, 29173−29183

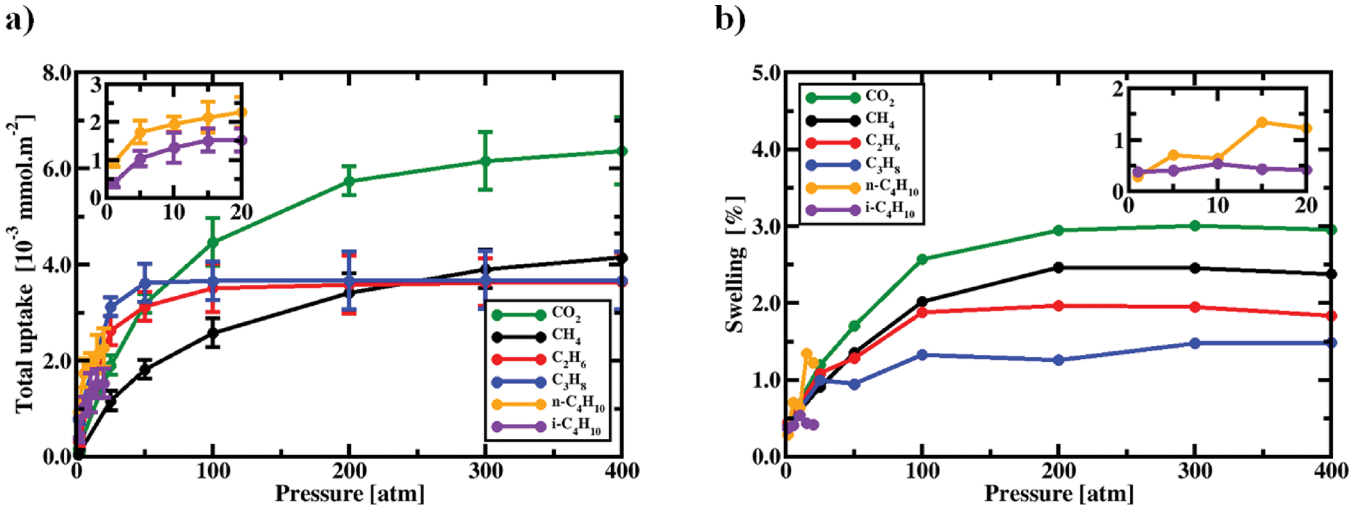

Figure 4. (a) Total uptake and (b) swelling vs pressure at T = 393.15 K in carbon dioxide (green), methane (black), ethane (red), propane (bleu), *n*-butane (orange), and *i*-butane (purple) in the flexible nailed kerogen matrices.

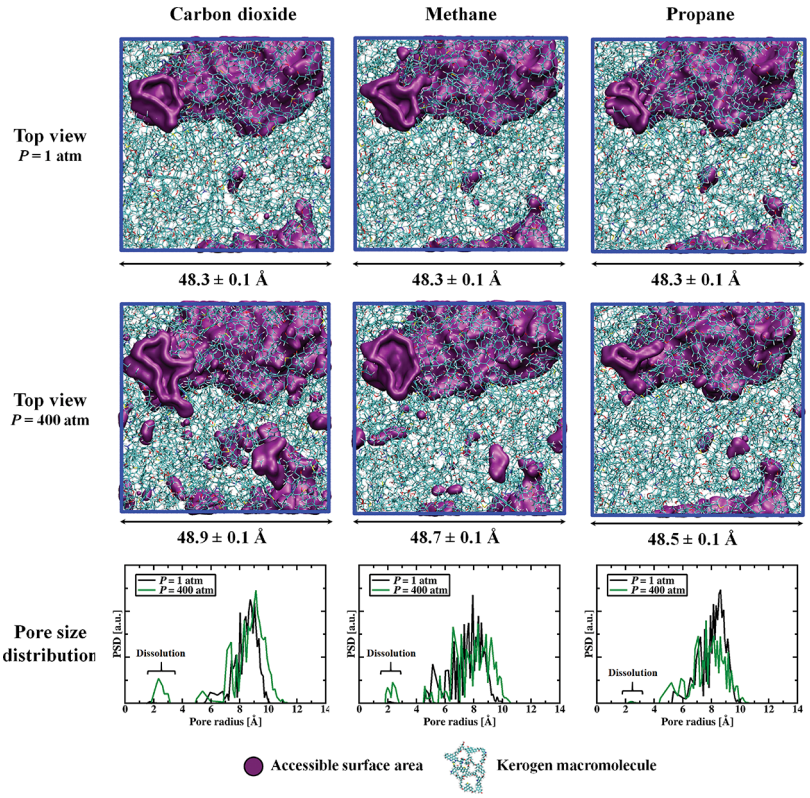

Figure 5. Top view of the accessible surface area and pore size distribution at T = 393.15 K and P = 1 and 400 atm in carbon dioxide, methane and propane. Note higher dissolution of CO_2 in kerogen matrix than methane, and less by propane at 400 atm.

K and 20 atm. This difference may be due to molecular volumes (45 ± 2 Å^3 for *n*-butane[95] and 58 ± 2 Å^3 for *i*-butane[95]) and molecular areas (20.5 ± 0.4 Å^2 for *n*-butane[95] and 21.9 ± 0.7 Å^2 for *i*-butane[95]). The same large difference is also reported in measurements using immature kerogen samples.[24−26]

Figure 4b shows that kerogen matrix swells more in adsorbates by smaller molecules (CO_2 > CH_4 > C_2H_6 > C_3H_8 at 393.15 K and 400 atm and *n*-C_4H_{10} > *i*-C_4H_{10} at 393.15 K and 20 atm). The flexibility of the kerogen matrix allows the kerogen microstructure to deform and to create paths. Small molecules can dissolve in the kerogen matrix. Pore size distribution in Figure 5 and the highlighted dissolved molecules in Figures S3 give strong evidence of dissolution (see the pore size distribution from adsorption of CO_2 and CH_4 in Figure 5) and creation of small pores by adsorption. These results demonstrate the need for considering kerogen flexibility in kerogen swelling and adsorption simulations.[24−26]

Structural Characterization. We have analyzed kerogen porosity and accessible surface area in flexible kerogen matrix at T = 393.15 K to a pressure of 400 atm in CO_2, CH_4, C_2H_6, and C_3H_8 and to a pressure of 20 atm in *n*-C_4H_{10} and *i*-C_4H_{10}.

The initial kerogen structure porosity and accessible surface area are, respectively, 10.8 ± 0.2% and 360 ± 11 m^2 g^{-1} (Table

DOI: 10.1021/acs.jpcc.9b04592
J. Phys. Chem. C 2019, 123, 29173−29183

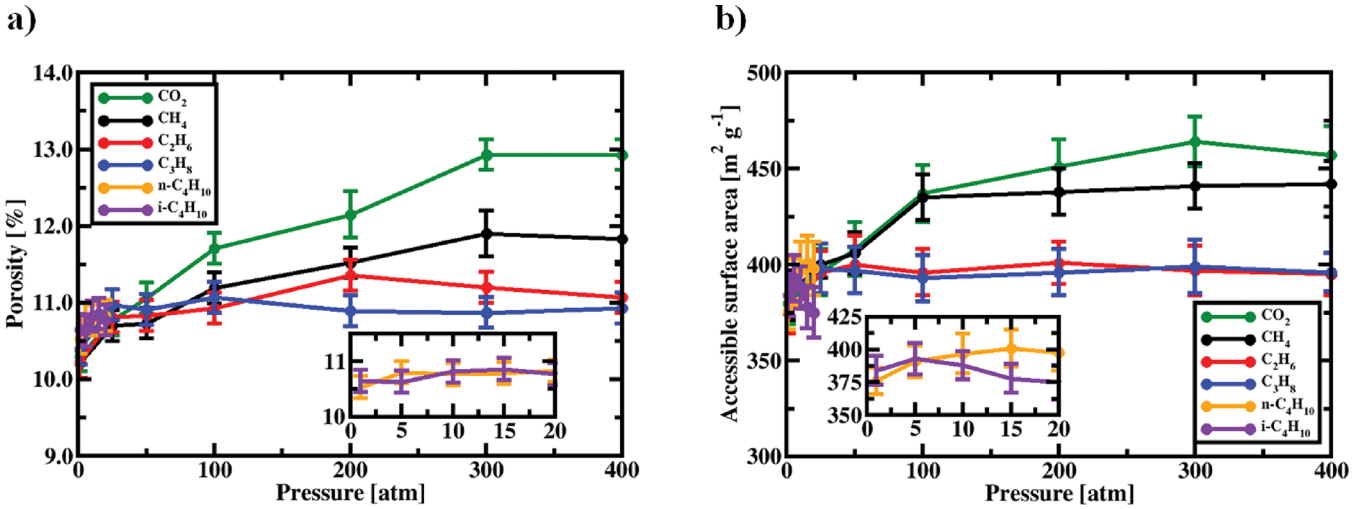

Figure 6. a) Porosity, and b) accessible surface area vs pressure at T = 393.15 K in carbon dioxide (green), methane (black), ethane (red), propane (bleu), *n*-butane (orange), and *i*-butane (purple) in the swollen nailed kerogen matrix.

2). Figure 6a shows that upon gas adsorption, in the flexible kerogen structure, the porosity increases to 12.9 ± 0.2% by CO_2, 11.8 ± 0.3% by CH_4, 11.1 ± 0.2% by C_2H_6, and 10.9 ± 0.2% by C_3H_8 at 400 atm. Whereas, in *n*-butane (10.8 ± 0.2%) and *i*-butane (10.8 ± 0.2%), the porosity fluctuates around the initial value from 1 to 20 atm. Figure 6b shows that from gas adsorption, the accessible surface area increases to 457 ± 15 m^2 g^{-1} by CO_2, 442 ± 12 m^2 g^{-1} by CH_4, 395 ± 11 m^2 g^{-1} by C_2H_6 and 396 ± 10 m^2 g^{-1} by C_3H_8 at 400 atm and to 398 ± 14 m^2 g^{-1} by *n*-C_4H_{10} and 375 ± 13 m^2 g^{-1} by *i*-C_4H_{10} at 20 atm. With increasing pressure, kerogen microstructure changes, the accessible surface increases and the kerogen swelling may generate larger pores (Figures 6a, b, S5, and S6). These results are in agreement with Ho et al.[49] in type II-D flexible kerogen matrix. In contrast to the work by Ho et al.[49] we find that small gas molecules can dissolve in the solid increasing the swelling of the kerogen matrix. Note the sudden change in the slope of the accessible surface area from 50 to 100 atm (Figure 6b). This is due to the fact that small gas molecules dissolve in the solid and create small pores. These results are in line with the pore size distribution (Figures 5 and S5). The increase in pressure results in swelling which allows gas to access spaces that it cannot at lower pressure. The kerogen molecular flexibility has a significant effect on adsorption and kerogen swelling.

CONCLUSIONS

In this work we have proposed a new method to create and engineer the kerogen porosity based on flexible kerogen macromolecules using a dummy particle and a limited number of nails to prevent the collapse of the pore structure of the kerogen. We use the type II-A kerogen macromolecules. Without the nails, the system would collapse and the porosity would decrease drastically. By using a dummy particle we create large enough pores to accommodate adsorption of methane, ethane, propane, *n*-butane, *i*-butane, carbon dioxide, and saturation by *n*-pentane. The method can be used with other types of kerogen molecules. The adsorption of CH_4, C_2H_6, C_3H_8, and CO_2 (393.15 K to a pressure of 400 atm), *n*-C_4H_{10} and *i*-C_4H_{10} (393.15 K to a pressure of 20 atm) and saturation by liquid *n*-C_5H_{12} (298.15 K and 1 atm) are predicted using the hybrid Molecular Dynamics-Grand Canonical Monte Carlo (MD-GCMC) method. The kerogen swelling is also investigated by MD-GCMC simulations. The key element of creating a kerogen matrix is the use of a limited number of nails to avoid porosity collapse. The use of the nail technique can be further refined to achieve full swelling in the future. The main findings from our work are

1. The flexibility of kerogen matrix allows the kerogen microstructure to deform and to create paths. Small molecules can dissolve in the kerogen matrix. Ethane and propane adsorption at 393.15 K reaches a plateau at ∼200 and ∼100 atm, respectively. Methane and carbon dioxide adsorption shows increasing trend even to 400 atm. Carbon dioxide adsorption is about ∼1.7 times higher than methane adsorption (mol basis) at 393.15 K and 400 atm.

2. Whereas *n*-butane and *i*-butane molecules have the same molecular weight and close bulk gas densities, *n*-butane adsorption is about ∼1.5 times higher than *i*-butane adsorption at 393.15 K and 20 atm.

3. Adsorption leads to structural change in the flexible kerogen matrix ; the swelling of the kerogen with gases decreases with increasing the size of the molecules (CO_2 > CH_4 > C_2H_6 > C_3H_8 at 393.15 K and 400 atm). The swelling has a monotonic increase with increase in pressure and may reach a plateau. It does not show a nonmonotonic trend with pressure as some literature suggests.

4. The process of swelling in the hydrocarbon liquid *n*-C_5H_{12} is different than that in hydrocarbon gases. The pore structure changes and porosity increases more significantly by the light hydrocarbon liquid *n*-C_5H_{12} than in gases.

In the future, we plan to further investigate the isothermal adsorptions of several hydrocarbons (from CH_4 to $C_{14}H_{30}$ using MD-GCMC and configurational bias-GCMC methods) and the system size effect by increasing the number of kerogen macromolecules and/or the number of dummy particles. Results will be published as they become available.

DOI: 10.1021/acs.jpcc.9b04592
J. Phys. Chem. C 2019, 123, 29173−29183

■ ASSOCIATED CONTENT

Supporting Information

The Supporting Information is available free of charge on the ACS Publications website at DOI: 10.1021/acs.jpcc.9b04592.

Composition and structural parameters of type II-A kerogen macromolecule, bulk density, hybrid simulations characteristics, structure characterization of the kerogen matrix based on the MD relaxation procedure without and with nails, structure characterization of the kerogen matrix at different pressures, box density, structure characterization of the kerogen matrix using the sequential and direct isotherm calculation approaches, pore size distribution of the kerogen matrix without and with nails at T = 298.15 K, front view of the simulation box and zoom on one nailed atom, top view of the simulation box with CO_2 and hydrocarbons (methane and propane) dissolved in an isolated micropore, average temperature, pressure, and number of *n*-butane molecules in the simulation box at 393.15 K and 20 atm, pore size distribution at three different pressures and T = 393.15 K, and views of the accessible surface area at P = 400 atm and T = 393.15 K (PDF)

■ AUTHOR INFORMATION

Corresponding Author

*Phone: +1 (650) 326-9172. E-mail: af@rerinst.org.

ORCID

Stéphane Tesson: 0000-0001-9045-1443

Abbas Firoozabadi: 0000-0001-6102-9534

Notes

The authors declare no competing financial interest.

■ ACKNOWLEDGMENTS

This research was supported by member companies of the Reservoir Engineering Research Institute (RERI). The support is greatly appreciated. S.T. would like to thank T. Wu and A. Gama Goicochea for discussions.

■ REFERENCES

(1) IEA. https://www.eia.gov, (accessed October 22, 2018).

(2) Ungerer, P.; Collell, J.; Yiannourakou, M. Molecular modeling of the volumetric and thermodynamic properties of kerogen: Influence of organic type and maturity. *Energy Fuels* **2015**, *29*, 91−105.

(3) Clarkson, C. R.; Solano, N.; Bustin, R. M.; Bustin, A. M. M.; Chalmers, G. R. L.; He, L.; Melnichenko, Y. B.; Radliński, A. P.; Blach, T. P. Pore structure characterization of north American shale gas reservoirs using USANS/SANS, gas adsorption, and mercury intrusion. *Fuel* **2013**, *103*, 606−616.

(4) Cao, T.; Song, Z.; Wang, S.; Cao, X.; Li, Y.; Xia, J. Characterizing the pore structure in the silurian and permian shales of the sichuan basin, china. *Mar. Pet. Geol.* **2015**, *61*, 140−150.

(5) Etminan, S. R.; Javadpour, F.; Maini, B. B.; Chen, Z. Measurement of gas storage processes in shale and of the molecular diffusion coefficient in kerogen. *Int. J. Coal Geol.* **2014**, *123*, 10−19.

(6) Durand, B. *Kerogen: Insoluble Organic Matter from Sedimentary Rocks*; Editions Technip, 1980.

(7) Sui, H.; Yao, J. Effect of surface chemistry for CH_4/CO_2 adsorption in kerogen: A molecular simulation study. *J. Nat. Gas Sci. Eng.* **2016**, *31*, 738−746.

(8) Orr, W. L. Kerogen/asphaltene/sulfur relationships in sulfur-rich monterey oils. *Org. Geochem.* **1986**, *10*, 499−516.

(9) Tissot, B. P.; Welte, D. H. In *Petroleum Formation and Occurrence*, 2nd revised ed.; Tokyo, B. H. N. Y., Ed.; Springer-Verlag: New York, 1984.

(10) Ganz, H.; Kalkreuth, W. Application of infrared spectroscopy to the classification of kerogentypes and the evaluation of source rock and oil shale potentials. *Fuel* **1987**, *66*, 708−711.

(11) Okiongbo, K. S.; Aplin, A. C.; Larter, S. R. Changes in type II kerogen density as a function of maturity: Evidence from the kimmeridge clay formation. *Energy Fuels* **2005**, *19*, 2495−2499.

(12) Tong, J.; Han, X.; Wang, S.; Jiang, X. Evaluation of structural characteristics of huadian oil shale kerogen using direct techniques (solid-state 13C NMR, XPS, FT-IR, and XRD). *Energy Fuels* **2011**, *25*, 4006−4013.

(13) Gasparik, M.; Ghanizadeh, A.; Bertier, P.; Gensterblum, Y.; Bouw, S.; Krooss, B. M. High-pressure methane sorption isotherms of black shales from the netherlands. *Energy Fuels* **2012**, *26*, 4995−5004.

(14) Yan, J.; Jiang, X.; Han, X.; Liu, J. A TG−FTIR investigation to the catalytic effect of mineral matrix in oil shale on the pyrolysis and combustion of kerogen. *Fuel* **2013**, *104*, 307−317.

(15) Charoensuppanimit, P.; Mohammad, S. A.; Gasem, K. A. M. Measurements and modeling of gas adsorption on shales. *Energy Fuels* **2016**, *30*, 2309−2319.

(16) Tian, H.; Li, T.; Zhang, T.; Xiao, X. Characterization of methane adsorption on overmature lower silurian−upper ordovician shales in sichuan basin, southwest china: Experimental results and geological implications. *Int. J. Coal Geol.* **2016**, *156*, 36−49.

(17) Ji, W.; Song, Y.; Rui, Z.; Meng, M.; Huang, H. Pore characterization of isolated organic matter from high matured gas shale reservoir. *Int. J. Coal Geol.* **2017**, *174*, 31−40.

(18) Pang, Y.; Soliman, M. Y.; Deng, H.; Xie, X. Experimental and analytical investigation of adsorption effects on shale gas transport in organic nanopores. *Fuel* **2017**, *199*, 272−288.

(19) Li, J.; Zhou, S.; Gaus, G.; Li, Y.; Ma, Y.; Chen, K.; Zhang, Y. Characterization of methane adsorption on shale and isolated kerogen from the Sichuan Basin under pressure up to 60 MPa: Experimental results and geological implications. *Int. J. Coal Geol.* **2018**, *189*, 83−93.

(20) Duan, X.; Hu, Z.; Gao, S.; Shen, R.; Liu, H.; Chang, J.; Wang, L. Shale high pressure isothermal adsorption curve and the production dynamic experiments of gas well. *Pet. Explor. Dev.* **2018**, *45*, 127−135.

(21) Zhou, S.; Xue, H.; Ning, Y.; Guo, W.; Zhang, Q. Experimental study of supercritical methane adsorption in longmaxi shale: Insights into the density of adsorbed methane. *Fuel* **2018**, *211*, 140−148.

(22) Hu, H.; Hao, F.; Guo, X.; Dai, F.; Lu, Y.; Ma, Y. Investigation of methane sorption of overmature wufeng-longmaxi shale in the jiaoshiba area, eastern sichuan basin, china. *Mar. Pet. Geol.* **2018**, *91*, 251−261.

(23) Rexer, T. F.; Mathia, E. J.; Aplin, A. C.; Thomas, K. M. High-pressure methane adsorption and characterization of pores in posidonia shales and isolated kerogens. *Energy Fuels* **2014**, *28*, 2886−2901.

(24) Zhao, H.; Lai, Z.; Firoozabadi, A. Sorption hysteresis of light hydrocarbons and carbon dioxide in shale and kerogen. *Sci. Rep.* **2017**, *7*, 16209.

(25) Zhao, H.; Wu, T.; Firoozabadi, A. High pressure sorption of various hydrocarbons and carbon dioxide in kimmeridge blackstone and isolated kerogen. *Fuel* **2018**, *224*, 412−423.

(26) Wu, T.; Zhao, H.; Tesson, S.; Firoozabadi, A. Absolute adsorption of light hydrocarbons and carbon dioxide in shale rock and and isolated kerogen. *Fuel* **2019**, *235*, 855−867.

(27) Fan, K.; Li, Y.; Elsworth, D.; Dong, M.; Yin, C.; Li, Y.; Chen, Z. Three stages of methane adsorption capacity affected by moisture content. *Fuel* **2018**, *231*, 352−360.

(28) Larsen, J. W.; Li, S. Solvent swelling studies of green river kerogen. *Energy Fuels* **1994**, *8*, 932−936.

(29) Larsen, J. W.; Li, S. Changes in the macromolecular structure of a type I kerogen during maturation. *Energy Fuels* **1997**, *11*, 897−901.

DOI: 10.1021/acs.jpcc.9b04592
J. Phys. Chem. C 2019, 123, 29173−29183

(30) Larsen, J. W.; Li, S. An initial comparison of the interactions of type I and III kerogens with organic liquids. *Org. Geochem.* **1997**, *26*, 305−309.
(31) Larsen, J. W.; Parikh, H.; Michels, R. Changes in the cross-link density of paris basin toarcian kerogen during maturation. *Org. Geochem.* **2002**, *33*, 1143−1152.
(32) Ballice, L. Solvent swelling studies of göynük (kerogen type-I) and beypazarı oil shales (kerogen type-II). *Fuel* **2003**, *82*, 1317−1321.
(33) Ertas, D.; Kelemen, S. R.; Halsey, T. C. Petroleum expulsion part 1. Theory of kerogen swelling in multicomponent solvents. *Energy Fuels* **2006**, *20*, 295−300.
(34) Kelemen, S. R.; Walters, C. C.; Ertas, D.; Kwiatek, L. M.; Curry, D. J. Petroleum expulsion part 2. Organic matter type and maturity effects on kerogen swelling by solvents and thermodynamic parameters for kerogen from regular solution theory. *Energy Fuels* **2006**, *20*, 301−308.
(35) Savest, N.; Oja, V.; Kaevand, T.; Lille, Ü. Interaction of estonian kukersite with organic solvents: A volumetric swelling and molecular simulation study. *Fuel* **2007**, *86*, 17−21.
(36) Savest, N.; Hruljova, J.; Oja, V. Characterization of thermally pretreated kukersite oil shale using the solvent-swelling technique. *Energy Fuels* **2009**, *23*, 5972−5977.
(37) Falk, K.; Pellenq, R.; Ulm, F. J.; Coasne, B. Effect of chain length and pore accessibility on alkane adsorption in kerogen. *Energy Fuels* **2015**, *29*, 7889−7896.
(38) Bousige, C.; Ghimbeu, C. M.; Vix-Guterl, C.; Pomerantz, A. E.; Suleimenova, A.; Vaughan, G.; Garbarino, G.; Feygenson, M.; Wildgruber, C.; Ulm, F.-J.; et al. Realistic molecular model of kerogen's nanostructure. *Nat. Mater.* **2016**, *15*, 576−582.
(39) Michalec, L.; Lísal, M. Molecular simulation of shale gas adsorption onto overmature type II model kerogen with control microporosity. *Mol. Phys.* **2017**, *115*, 1086−1103.
(40) Obliger, A.; Pellenq, R.; Ulm, F.-J.; Coasne, B. Free volume theory of hydrocarbon mixture transport in nanoporous materials. *J. Phys. Chem. Lett.* **2016**, *7*, 3712−3717.
(41) Ho, T. A.; Criscenti, L. J.; Wang, Y. Nanostructural control of methane release in kerogen and its implications to wellbore production decline. *Sci. Rep.* **2016**, *6*, 28053.
(42) Feng, F.; Akkutlu, I. Y. Molecular modeling of organic materials for flow simulation and digital source-rock physics. In *SPE Annual Technical Conference and Exhibition*; 2017.
(43) Pathak, M.; Kweon, H.; Deo, M.; Huang, H. Kerogen swelling and confinement: Its implication on fluid thermodynamic properties in shales. *Sci. Rep.* **2017**, *7*, 12530.
(44) Pathak, M.; Huang, H.; Meakin, P.; Deo, M. Molecular investigation of the interactions of carbon dioxide and methane with kerogen: Application in enhanced shale gas recovery. *J. Nat. Gas Sci. Eng.* **2018**, *51*, 1−8.
(45) Vasileiadis, M.; Peristeras, L. D.; Papavasileiou, K. D.; Economou, I. G. Modeling of bulk kerogen porosity: Methods for control and characterization. *Energy Fuels* **2017**, *31*, 6004−6018.
(46) Wang, Z.; Li, Y.; Liu, H.; Zeng, F.; Guo, P.; Jiang, W. Study on the adsorption, diffusion and permeation selectivity of shale gas in organics. *Energies* **2017**, *10*, 142.
(47) Zhao, T.; Li, X.; Zhao, H.; Li, M. Molecular simulation of adsorption and thermodynamic properties on type II kerogen: Influence of maturity and moisture content. *Fuel* **2017**, *190*, 198−207.
(48) Zhao, T.; Li, X.; Ning, Z.; Zhao, H.; Li, M. Molecular simulation of methane adsorption on type II kerogen with the impact of water content. *J. Pet. Sci. Eng.* **2018**, *161*, 302−310.
(49) Ho, T. A.; Wang, Y.; Criscenti, L. J. Chemo-mechanical coupling in kerogen gas adsorption/desorption. *Phys. Chem. Chem. Phys.* **2018**, *20*, 12390−12395.
(50) Huang, L.; Ning, Z.; Wang, Q.; Qi, R.; Zeng, Y.; Qin, H.; Ye, H.; Zhang, W. Molecular simulation of adsorption behaviors of methane, carbon dioxide and their mixtures on kerogen: Effect of kerogen maturity and moisture content. *Fuel* **2018**, *211*, 159−172.
(51) Obliger, A.; Ulm, F.-J.; Pellenq, R. J.-M. Impact of nanoporosity on hydrocarbon transport in shales' organic matter. *Nano Lett.* **2018**, *18*, 832−837.
(52) Vasileiadis, M.; Peristeras, L. D.; Papavasileiou, K. D.; Economou, I. G. Transport properties of shale gas in relation to kerogen porosity. *J. Phys. Chem. C* **2018**, *122*, 6166−6177.
(53) Wang, T.; Tian, S.; Li, G.; Sheng, M.; Ren, W.; Liu, Q.; Zhang, S. Molecular simulation of CO_2/CH_4 competitive adsorption on shale kerogen for CO_2 sequestration and enhanced gas recovery. *J. Phys. Chem. C* **2018**, *122*, 17009−17018.
(54) Perez, F.; Devegowda, D. Spatial distribution of reservoir fluids in mature kerogen using molecular simulations. *Fuel* **2019**, *235*, 448−459.
(55) Collell, J.; Galliero, G.; Gouth, F.; Montel, F.; Pujol, M.; Ungerer, P.; Yiannourakou, M. Molecular simulation and modelisation of methane/ethane mixtures adsorption onto a microporous molecular model of kerogen under typical reservoir conditions. *Microporous Mesoporous Mater.* **2014**, *197*, 194−203.
(56) Huang, L.; Ning, Z.; Li, H.; Wang, Q.; Ye, H.; Qin, H. Molecular simulation of CO_2 sequestration and enhanced gas recovery in gas rich shale: An insight based on realistic kerogen model. In *SPE Abu Dhabi International Petroleum Exhibition & Conference*; 2017.
(57) Huang, L.; Ning, Z.; Wang, Q.; Zhang, W.; Cheng, Z.; Wu, X.; Qin, H. Effect of organic type and moisture on CO_2/CH_4 competitive adsorption in kerogen with implications for CO_2 sequestration and enhanced CH_4 recovery. *Appl. Energy* **2018**, *210*, 28−43.
(58) Huang, L.; Ning, Z.; Wang, Q.; Ye, H.; Wang, Z.; Sun, Z.; Qin, H. Microstructure and adsorption properties of organic matter in chinese cambrian gas shale: Experimental characterization, molecular modeling and molecular simulation. *Int. J. Coal Geol.* **2018**, *198*, 14−28.
(59) Zhou, W.; Zhang, Z.; Wang, H.; Yan, Y.; Liu, X. Molecular insights into competitive adsorption of CO_2/CH_4 mixture in shale nanopores. *RSC Adv.* **2018**, *8*, 33939−33946.
(60) Song, R.; Cui, M. Molecular simulation on competitive adsorption mechanism of CH_4/CO_2 on shale kerogen. *Arabian J. Geosci.* **2018**, *11*, 403.
(61) Wang, H.; Qu, Z.; Yin, Y.; Bai, J.; Yu, B. Review of molecular simulation method for gas adsorption/desorption and diffusion in shale matrix. *J. Therm. Sci.* **2019**, *28*, 1−16.
(62) Tesson, S.; Firoozabadi, A. Methane adsorption and self-diffusion in shale kerogen and slit nanopores by molecular simulations. *J. Phys. Chem. C* **2018**, *122*, 23528−23542.
(63) Zhou, B.; Xu, R.; Jiang, P. Novel molecular simulation process design of adsorption in realistic shale kerogen spherical pores. *Fuel* **2016**, *180*, 718−726.
(64) Collell, J.; Ungerer, P.; Galliero, G.; Yiannourakou, M.; Montel, F.; Pujol, M. Molecular simulation of bulk organic matter in type II shales in the middle of the oil formation window. *Energy Fuels* **2014**, *28*, 7457−7466.
(65) Herrera, L.; Do, D. D.; Nicholson, D. A monte carlo integration method to determine accessible volume, accessible surface area and its fractal dimension. *J. Colloid Interface Sci.* **2010**, *348*, 529−536.
(66) Kazemi, M.; Maleki, H.; Takbiri-Borujeni, A. Molecular dynamics study of transport and storage of methane in kerogen. In *SPE Eastern Regional Meeting*; 2016.
(67) Trewin, A.; Willock, D. J.; Cooper, A. I. Atomistic simulation of micropore structure, surface area, and gas sorption properties for amorphous microporous polymer networks. *J. Phys. Chem. C* **2008**, *112*, 20549−20559.
(68) Brochard, L.; Vandamme, M.; Pellenq, R. J.-M.; Fen-Chong, T. Adsorption-induced deformation of microporous materials: Coal swelling induced by CO_2-CH_4 competitive adsorption. *Langmuir* **2012**, *28*, 2659−2670.
(69) Brochard, L.; Vandamme, M.; Pellenq, R. J.-M. Poromechanics of microporous media. *J. Mech. Phys. Solids* **2012**, *60*, 606−622.

DOI: 10.1021/acs.jpcc.9b04592
J. Phys. Chem. C 2019, 123, 29173−29183

(70) Wu, C.; Yang, D.-S. Effect of microstructural flexibility on methane flow in kerogen matrix by molecular dynamics simulations. *J. Phys. Chem. C* **2019**, *123*, 22390−22396.
(71) *MedeA*, version 2.22. Materials Design Inc.: Angel Fire, NM. http://www.materialsdesign.com, (accessed May 1, 2017).
(72) Sun, H.; Mumby, S. J.; Maple, J. R.; Hagler, A. T. An ab initio CFF93 all-atom force field for polycarbonates. *J. Am. Chem. Soc.* **1994**, *116*, 2978−2987.
(73) Sun, H. Ab initio calculations and force field development for computer simulation of polysilanes. *Macromolecules* **1995**, *28*, 701−712.
(74) Yiannourakou, M.; Ungerer, P.; Leblanc, B.; Rozanska, X.; Saxe, P.; Vidal-Gilbert, S.; Gouth, F.; Montel, F. Molecular simulation of adsorption in microporous materials. *Oil Gas Sci. Technol.* **2013**, *68*, 977−994.
(75) Sun, H.; Ren, P.; Fried, J. R. The COMPASS force field: Parameterization and validation for phosphazenes. *Comput. Theor. Polym. Sci.* **1998**, *8*, 229−246.
(76) Sun, H. COMPASS: An ab initio force-field optimized for condensed-phase applications overview with details on alkane and benzene compounds. *J. Phys. Chem. B* **1998**, *102*, 7338−7364.
(77) Bunte, S. W.; Sun, H. Molecular modeling of energetic materials: The parameterization and validation of nitrate esters in the COMPASS force field. *J. Phys. Chem. B* **2000**, *104*, 2477−2489.
(78) Yang, J.; Ren, Y.; Tian, A.-M.; Sun, H. COMPASS force field for 14 inorganic molecules, He, Ne, Ar, Kr, Xe, H_2, O_2, N_2, NO, CO, CO_2, NO_2, CS_2, and SO_2, in liquid phases. *J. Phys. Chem. B* **2000**, *104*, 4951−4957.
(79) McQuaid, M. J.; Sun, H.; Rigby, D. Development and validation of COMPASS force field parameters for molecules with aliphatic azide chains. *J. Comput. Chem.* **2004**, *25*, 61−71.
(80) Waldman, M.; Hagler, A. T. New combining rules for rare gas van der waals parameters. *J. Comput. Chem.* **1993**, *14*, 1077−1084.
(81) Frenkel, D.; Smit, B. *Understanding Molecular Simulation: From Algorithms to Applications*; Academic Press, 2001; Vol. *1*.
(82) Plimpton, S. Fast parallel algorithms for short-range molecular dynamics. *J. Comput. Phys.* **1995**, *117*, 1−19.
(83) Nosé, S. A unified formulation of the constant temperature molecular. *J. Chem. Phys.* **1984**, *81*, 511−519.
(84) Nosé, S. A molecular dynamics method for simulations in the canonical ensemble. *Mol. Phys.* **1984**, *52*, 255−268.
(85) Nosé, S.; Klein, M. L. A study of solid and liquid carbon tetrafluoride using the constant pressure molecular dynamics technique. *J. Chem. Phys.* **1983**, *78*, 6928−6939.
(86) Hoover, W. G. Constant-pressure equations of motion. *Phys. Rev. A: At., Mol., Opt. Phys.* **1986**, *34*, 2499−2500.
(87) Chempath, S.; Clark, L. A.; Snurr, R. Q. Two general methods for grand canonical ensemble simulation of molecules with internal flexibility. *J. Chem. Phys.* **2003**, *118*, 7635−7643.
(88) Koretsky, M. D. *Engineering and Chemical Thermodynamics*; John Wiley & Sons, 2012.
(89) Barnes, C. S. ThermoSolver: An integrated educational thermodynamics software program. Ph.D. thesis, Oregon State University, 2006.
(90) Düren, T.; Millange, F.; Férey, G.; Walton, K. S.; Snurr, R. Q. Calculating geometric surface areas as a characterization tool for metal-organic frameworks. *J. Phys. Chem. C* **2007**, *111*, 15350−15356.
(91) Bhattacharya, S.; Gubbins, K. E. Fast method for computing pore size distributions of model materials. *Langmuir* **2006**, *22*, 7726−7731.
(92) de León-Barreneche, J.; Hoyos-Madrigal, B. A.; Cañas-Marín, W. A. Aggregation study of asphaltenes from colombian castilla crude oil using molecular simulation. *Revista Facultad de Ingeniería Universidad de Antioquia* 2015, 25−31.
(93) Firoozabadi, A. *Thermodynamics and Applications of Hydrocarbon Energy Production*; McGraw Hill Professional, 2015.
(94) Pang, Y.; Tian, Y.; Soliman, M. Y.; Shen, Y. Experimental measurement and analytical estimation of methane absorption in shale kerogen. *Fuel* **2019**, *240*, 192−205.
(95) Brown, T. C. Adsorption properties from pressure-varying langmuir parameters: n-Butane and isobutane on activated carbon. *Energy Fuels* **2017**, *31*, 2109−2117.

NOTE ADDED AFTER ASAP PUBLICATION

This article published November 14, 2019 with a missing affiliation for Abbas Firoozabadi. The affiliation was added and the article reposted November 19, 2019.

DOI: 10.1021/acs.jpcc.9b04592
J. Phys. Chem. C 2019, 123, 29173−29183